Experimental Elastic Deformation Characterization of a Flapping-Wing MAV using Visual Image Correlation

Kelly C. Stewart* and Roberto Albertani†
Research and Engineering Education Facility, University of Florida, Shalimar, FL, 32579

This paper presents a method for using visual image correlation (VIC) data to decouple the rigid-body-motion of a flexible wing from elastic deformation. Estimating the elastic deformation can be used to gain insight into the unsteady aerodynamics associated with flapping flight. By making use of a dynamic VIC system, which measures the full-field displacements, the entire flapping motion for a wing can be measured. If the experiment is setup carefully, the combination of the rigid-body-motion and motion due to flexibility can be measured simultaneously for a single specimen. Discussed in this paper is a method for determining the homogeneous transformation matrix (HTM) associated with the rigid-body-motion. The HTM is used to project the rigid body motion to the flexible portions of the wing, thereby, separating the elastic deformation from the total wing displacement. A series of static tests involving known rotations and deformations were carried out to test the method. Following validation, the method was applied to VIC data from two different flexible, flapping wings and contours of the wing deformations were successfully generated.

Nomenclature

HTM	=	homogeneous transformation matrix
R_x, R_y, R_z	=	rotations about the x-, y-, and z-axes, respectively
t_x, t_y, t_z	=	translations in the x-, y-, and z-directions, respectively
u, v, w	=	displacements in the x-, y-, and z-directions, respectively
u_{HTM}	=	uncertainty in the homogenous transformation matrix
u_u, u_v, u_w	=	uncertainty in the displacement measurements
u_Γ, u_Ψ, u_Θ	=	uncertainty in the rotation angles
X, Y, Z	=	reference location in the x-, y-, and z-direction, respectively
θ_{HTM}	=	sensitivity of the rotation angles to the homogenous transformation matrix
Γ	=	flapping angle (rotation about y axis)
Ψ	=	sweep angle (rotation about z axis)
Θ	=	feather angle (rotation about x axis)

I. Introduction

THERE is interest in the research community to further develop the technologies associated with micro air vehicles (MAVs) and their ability to perform in tightly confined environments at widely varying flight conditions. Such applications require that MAVs be highly agile and adaptable, much like the natural fliers seen today. In the pursuit of improving MAV flying capabilities, engineers have turned to biology[1,2] for inspiration. One common characteristic seen among natural fliers capable of highly agile and versatile flight is flexibility. Wing flexibility allows fliers to readily adapt to changing flight conditions, either through passive mechanisms such as adaptive washout or by active morphing of the wing shape to increase lift. Flexibility is also exploited by marine mammals in the generation of thrust[3]. Cetaceans rotate their flukes during the swimming motion to keep a positive angle-of-attack with respect to the water flow. This rotation changes the camber of the flukes, which increases the lift and thrust. Fixed-wing MAVs whose wing structures are fabricated of an aeroelastic

* Masters Student, University of Florida, 101 West Eglin Blvd, Eglin AFB, FL, 32542.
† Visiting Professor, Research and Engineering Education Facility, University of Florida, 1350 North Poquito Rd, Shalimar, FL, 32579.

material have been shown to have advantages over their rigid counterparts, particularly in regards to the improved pitching moment curve and ability to store energy that would normally be lost to wing-tip vortices and wake[4].

While flexible fixed-wings do have an advantage over rigid ones, they still do not meet all of the agility and versatility requirements for low-speed flight in constricted environments. Biology has shown that natural fliers who fly at low speeds use flapping rather than fixed-wings. This is seen in birds, bats, and insects. Bats, in particular, showcase extremely complex wing motion that enables them to execute highly agile maneuvers in very small spaces[5]. Natural fliers make use of resonant excitation to flap their wings efficiently at high frequencies and vary the wing beat between flight modes[2].

With the many examples of natural fliers exploiting flexible, flapping wings[6], it is worth investigating the kinematics and dynamics of such motion. The wing kinematics and dynamics need to be decoupled when applying biologically-inspired technologies to MAVs. For instance, the IMU and system identification only require knowing the rigid-body-motion. However, combining the wing mechanics of flexible wings[7] with feedback control similar to that seen in biological organisms requires knowing the elastic deformation. A dynamic visual-image-correlation system provides a means for simultaneously measuring both rigid-body-motion and deformation and is already being used extensively on flexible, fixed-wing MAVs, as documented in Ref. 4. The method for setting up flapping-wing VIC experiments and estimating the elastic deformation using the data obtained is presented in this paper.

II. Methodology

Visual image correlation (VIC) provides a means of measuring in-plane and out-of-plane displacements for a test specimen undergoing any combination of motion and deformation. The technique originated from the University of South Carolina under the work of Dr. M. Sutton[8,9]. It uses stereo triangulation to measure the displacement of points on a surface over time. Stereo triangulation requires the test specimen to be covered in a random, speckled pattern with as little glare as possible. Snapshots of the specimen are taken by high-speed cameras and processed through the VIC software where the movement of each speckle is tracked. This, in turn, provides the motion and deformation of the specimen.

Given a flexible wing, if VIC data for a rigid portion of the wing is available, it is possible to estimate the complete set of rotations and translations describing the wing motion. To achieve the above result, the homogeneous transformation matrix[10] (HTM) describing the rigid body motion must be solved for. By knowing the starting reference point and the final position after displacement, the elements of the HTM can be found using a best-fit method for the entire area-of-interest (AOI). The area-of-interest pertains to the portion of the wing which is selected for image correlation. Definitions for the rotation angles and translations are presented in Figure 1 – Figure 4.

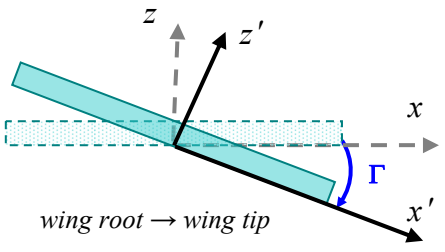

Figure 1. Definition of flapping angle, Γ.

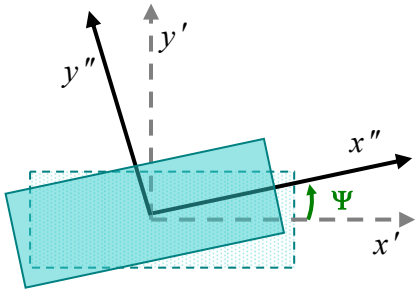

Figure 2. Definition of sweep angle, Ψ.

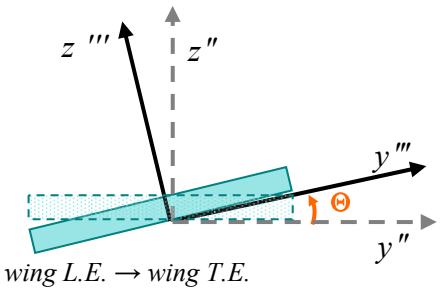

Figure 3. Definition of feather angle, Θ.

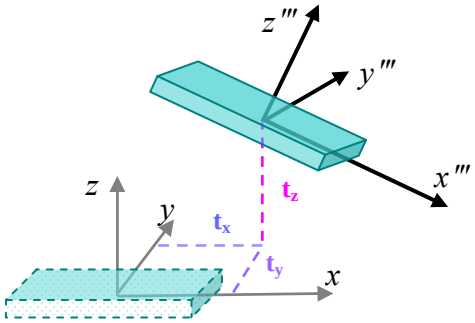

Figure 4. Translations pertaining to the displacement of the AOI centroid.

The HTM describes the motion of the AOI about its origin: the centroid of the AOI prior to wing movement. It is constructed by premultiplying four homogeneous matrices: three for the angles of rotation (Γ,Θ, Ψ) and one for the translation (t_x, t_y, t_z). Order of multiplication is important when dealing with matrices. For this experiment, it will be assumed the y-axis rotation occurs first, followed by the z'-axis rotation, and then the x"-axis rotation. This gives the following transformation matrix,

$$HTM = T \cdot R_x(\Theta) \cdot R_z(\Psi) \cdot R_y(\Gamma) \tag{1}$$

$$HTM = \begin{bmatrix} \cos\Gamma\cos\Psi & -\sin\Psi & \sin\Gamma\cos\Psi & t_x \\ \cos\Gamma\sin\Psi\cos\Theta + \sin\Gamma\sin\Theta & \cos\Psi\cos\Theta & \sin\Gamma\sin\Psi\cos\Theta - \cos\Gamma\sin\Theta & t_y \\ \cos\Gamma\sin\Psi\sin\Theta - \sin\Gamma\cos\Theta & \cos\Psi\sin\Theta & \sin\Gamma\sin\Psi\sin\Theta + \cos\Gamma\cos\Theta & t_z \\ 0 & 0 & 0 & 1 \end{bmatrix} \tag{2}$$

Applying the HTM across the points in the AOI, equations for the displacement along each axis can be written as,

$$\begin{bmatrix} X+u \\ Y+v \\ Z+w \\ 1 \end{bmatrix}_i^{x,y,z} = [HTM] \begin{bmatrix} X \\ Y \\ Z \\ 1 \end{bmatrix}_i^{x,y,z} \quad \text{where i} = 1,\ldots,N_{\text{data points}} \tag{3}$$

The displacement equations can be restructured into the form **b** = A**x** where **b** is a vector of VIC measurements, A is a matrix of the known reference points, and **x** corresponds to a row of elements in the HTM (see Eqn. 4). It is the elements of the HTM that are unknown and must be solved for.

$$\underset{N\,x\,1}{\left[\bar{X}+\bar{u}\right]} = \underset{N\,x\,4}{\left[\bar{X} \quad \bar{Y} \quad \bar{Z} \quad \bar{1}\right]} \underset{4\,x\,1}{\begin{bmatrix} \cos\Gamma\cos\Psi \\ -\sin\Psi \\ \sin\Gamma\cos\Psi \\ t_x \end{bmatrix}} = \underset{N\,x\,4}{\left[\bar{X} \quad \bar{Y} \quad \bar{Z} \quad \bar{1}\right]} \underset{4\,x\,1}{\begin{bmatrix} HTM_{11} \\ HTM_{12} \\ HTM_{13} \\ HTM_{14} \end{bmatrix}}$$

$$\underset{N\,x\,1}{\left[\bar{Y}+\bar{v}\right]} = \underset{N\,x\,4}{\left[\bar{X} \quad \bar{Y} \quad \bar{Z} \quad \bar{1}\right]} \underset{4\,x\,1}{\begin{bmatrix} \cos\Gamma\sin\Psi\cos\Theta + \sin\Gamma\sin\Theta \\ \cos\Psi\cos\Theta \\ \sin\Gamma\sin\Psi\cos\Theta - \cos\Gamma\sin\Theta \\ t_y \end{bmatrix}} = \underset{N\,x\,4}{\left[\bar{X} \quad \bar{Y} \quad \bar{Z} \quad \bar{1}\right]} \underset{4\,x\,1}{\begin{bmatrix} HTM_{21} \\ HTM_{22} \\ HTM_{23} \\ HTM_{24} \end{bmatrix}} \tag{4}$$

$$\underset{N\,x\,1}{\left[\overline{Z}+\overline{w}\right]}=\underset{N\,x\,4}{\left[\overline{X}\quad\overline{Y}\quad\overline{Z}\quad\overline{1}\right]}\begin{bmatrix}\cos\Gamma\sin\Psi\sin\Theta-\sin\Gamma\cos\Theta\\ \cos\Psi\sin\Theta\\ \sin\Gamma\sin\Psi\sin\Theta+\cos\Gamma\cos\Theta\\ t_z\end{bmatrix}_{4\,x\,1}=\underset{N\,x\,4}{\left[\overline{X}\quad\overline{Y}\quad\overline{Z}\quad\overline{1}\right]}\begin{bmatrix}HTM_{31}\\ HTM_{32}\\ HTM_{33}\\ HTM_{34}\end{bmatrix}_{4\,x\,1}$$

These matrices can easily be programmed into MATLAB and a least-squares regression used to arrive at the values of HTM_{ij} that yield the best match to the solution, **b**. The coefficients HTM_{i4}, where i=1,…,3, are the three translations. The remaining coefficients, HTM_{ij}, where i=1,…,3 and j=1,…,3, are the trigonometric functions of the rotation angles. By knowing the values of the coefficients, HTM_{ij}, that make up the transformation matrix, extracting the rotation angles is relatively straightforward through inverse trigonometry. The question is which elements of the HTM matrix should be used. Mathematically, using any combination of the elements should yield the same rotation angles. However, it will be discussed in a later section that errors arising from noise and from scaling issues will make some choices better than others. Presented below are the equations for acquiring the rotation angles from the first two columns of the HTM.

$$\Theta=\tan^{-1}\left(\frac{HTM_{32}}{HTM_{22}}\right)$$

$$\Psi=\tan^{-1}\left(\frac{-HTM_{12}}{HTM_{22}\cos\Theta+HTM_{32}\sin\Theta}\right) \tag{5}$$

$$\Gamma=\tan^{-1}\left(\frac{-HTM_{31}\cos\Theta+HTM_{21}\sin\Theta}{HTM_{11}/\cos\Psi}\right)$$

When analyzing data from the flexible portion of a specimen, it is understood the total displacements of the AOI include elastic deformation on top of the rigid-body-motion. By defining $\hat{x},\hat{y},\hat{z}$ as the frame of reference for the flexible AOI, then,

$$\begin{bmatrix}X+u\\ Y+v\\ Z+w\\ 1\end{bmatrix}_i^{\hat{x},\hat{y},\hat{z}}=\underbrace{\left[HTM\right]\begin{bmatrix}X\\ Y\\ Z\\ 1\end{bmatrix}_i^{\hat{x},\hat{y},\hat{z}}}_{Rigid\ Body\ Motion}+\underbrace{\begin{bmatrix}u_E\\ v_E\\ w_E\\ 1\end{bmatrix}_i^{\hat{x},\hat{y},\hat{z}}}_{Elastic\ Deformation} \tag{6}$$

The transformation matrix, HTM, based on the rigid AOI, can be used to project the rigid-body-motion to the flexible AOI. Care must be taken to transform the (X,Y,Z) coordinates of the flexible AOI to the rigid AOI reference frame, x,y,z, prior to applying the transformation matrix. Assuming $\hat{x},\hat{y},\hat{z}$ is not rotated with respect to x,y,z, then this is accomplished through simple translation. Otherwise, rotation must be taken into account and will require careful setup of the experiment to know the orientation of the flexible AOI reference frame with respect to the rigid. Equation 7 shows the complete homogeneous transformation matrix, where T_f represents the translation to the origin of the rigid AOI and HTM_0 is the transformation matrix at that origin.

$$HTM=\left[-T_f\right]_{x,y,z}^{\hat{x},\hat{y},\hat{z}}\ \left[\ HTM_0\right]\left[T_f\right]_{\hat{x},\hat{y},\hat{z}}^{x,y,z} \tag{7}$$

Finally, the rigid-body-motion is calculated using the HTM, and the result subtracted from the total displacement. The remaining values represent the elastic deformations (see Eqn. 8).

$$\begin{bmatrix} u_E \\ v_E \\ w_E \\ 1 \end{bmatrix}_i^{\hat{x},\hat{y},\hat{z}} = \underbrace{\begin{bmatrix} X+u \\ Y+v \\ Z+w \\ 1 \end{bmatrix}_i^{\hat{x},\hat{y},\hat{z}}}_{complete\ \ motion} - \underbrace{[HTM]\begin{bmatrix} X \\ Y \\ Z \\ 1 \end{bmatrix}_i^{\hat{x},\hat{y},\hat{z}}}_{rigid\ \ body\ \ motion} \tag{8}$$

III. Validation

A series of tests performed under static conditions were used to test the validity of estimating the HTM. For each test, a carbon fiber wing was positioned at a known rotation angle with a known deformation applied at the tip of the wing (see Figure 5). The objective was to apply the HTM algorithm and estimate the rotation angle and tip deformation solely based on the VIC data. In each test case, the starting reference position was set to 0° rotation and no deformation. Rotation angles were applied by mounting the wing vertically on a turntable incrementally marked in degrees. A caliper mounted vertically and affixed to the lab table by a magnet was used to apply the wing tip deformation at maximum span. During this experiment, repetition tests at three separate angles, with no tip deformation, were carried out to estimate the uncertainty in the displacement measurements. These tests each consisted of 50 snapshots taken with the wing held fixed. Any non-zero values for the measured displacements were considered errors.

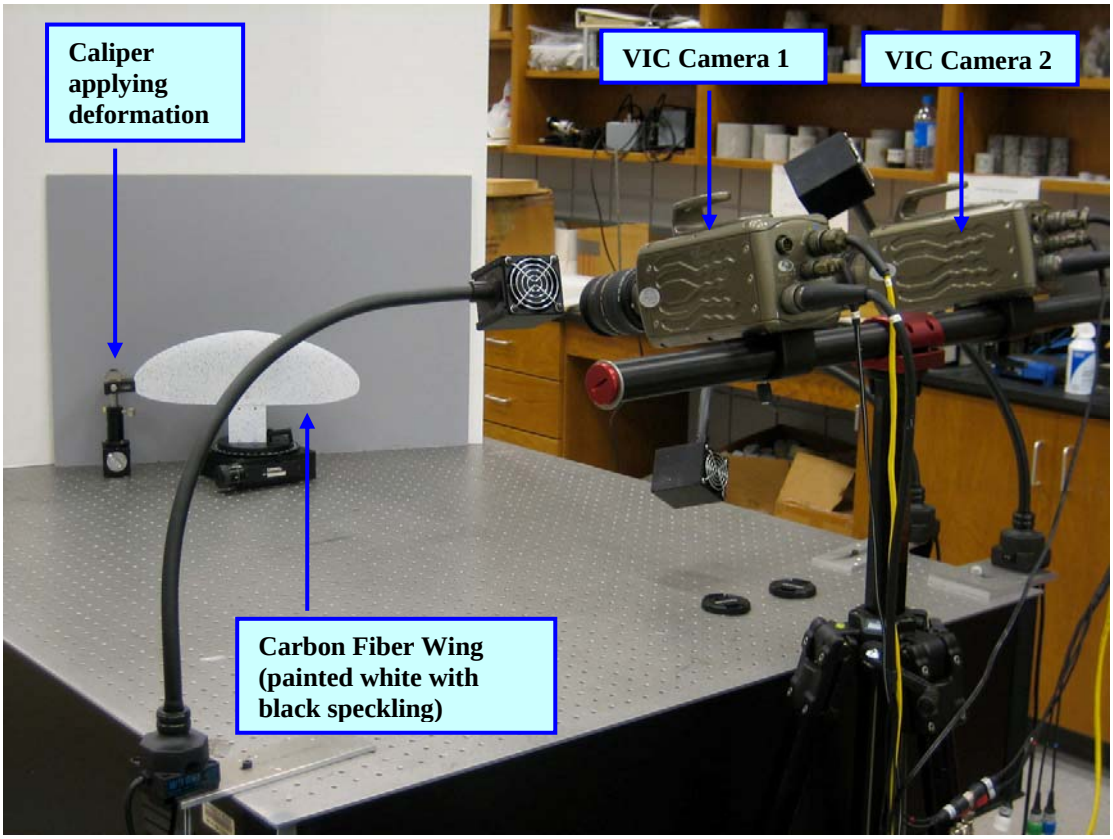

Figure 5. Experiment setup for the validation tests.

In order for the HTM algorithm to work, both a rigid and a flexible AOI are needed. In this case, the rigid AOI was considered to be the flat plate upon which the wing was mounted. Shown in Table 1 are the applied rotations and deformations. The resulting rotation angle estimates had errors on the order of 0.2°. The estimates of the deformation were off by 0.3 to 0.9 mm, however, it should be noted that the area-of-interest for these tests did not extend completely out to the tip of the wing span. Therefore, the estimated tip deformations actually correspond to a location just before the applied deformation.

Table 1. Text matrix for Validation of HTM Algorithm

Rotation, Γ [°]	*10*			*20*			*30*		
Tip Deformation [mm]	*2*	*4*	*6*	*2*	*4*	*6*	*2*	*4*	*6*

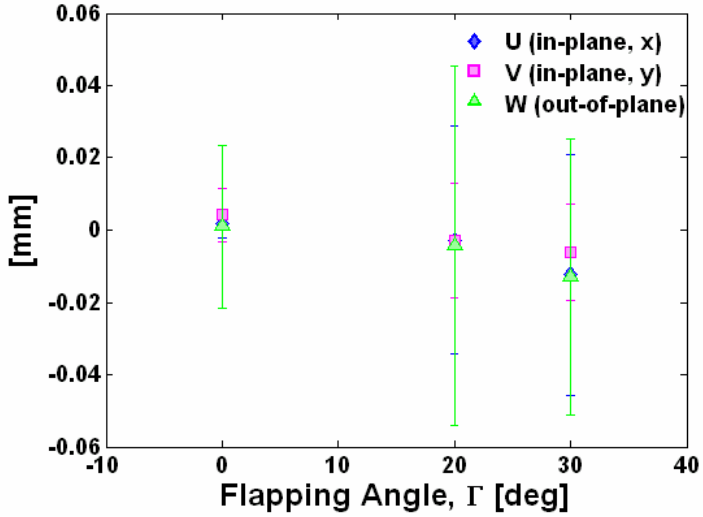

Figure 6. Mean Error and Standard Deviation of Measured Displacement.

Two observations were made during the validation and repetition tests. First, the magnitude of the mean measurement error increases with the flapping angle, as seen in Figure 6. The error magnitude ranges from 1.82e-03 to 1.29e-02 mm. Vertical bars in the figure represent the standard deviation of the mean error with the out-of-plane displacement showing the largest standard deviation. Secondly, due to the error in the measurements, it is sometimes possible for the estimated HTM elements to have values that fall just outside of the trigonometric domains (i.e. slightly greater than 1). For instance, in the test case of a 10° rotation, the element of the HTM that corresponded to $\cos(\Psi)\cos(\Theta)$ was estimated as 1.0007 (recall, both Ψ and Θ were 0° and, thus, this value should have been 1). A tolerance was applied by assuming values greater than 0.999 can be approximated as 1.0 to avoid processing errors during program execution. It is anticipated this does not significantly affect the data-processing results.

IV. Dynamic Tests

A. Experimental Setup

Having validated the mathematics behind the HTM algorithm, a second experiment was carried out under dynamic conditions. In this experiment, two different wings, both composed of rigid and flexible parts, were subjected to a flapping motion. Measurements with the VIC system were used to extract both the kinematic motion of the wings and the deformations. The first wing was acquired from a commercially available vehicle which is capable of flapping flight. A kite-like material that does not stretch is placed over carbon fiber rods to form the wing (see Figure 7). During discussion of the experiment and results, this wing will be referred to as the kite wing. The second wing was fabricated at the MAV Lab at the University of Florida in Gainesville. It is composed of thin latex stretched over a carbon fiber frame (see Figure 8). The latex is 0.33 mm thick and can stretch significantly. The wing perimeter is made with bidirectional carbon fiber while the battens are unidirectional. This wing will be referred to as the latex wing.

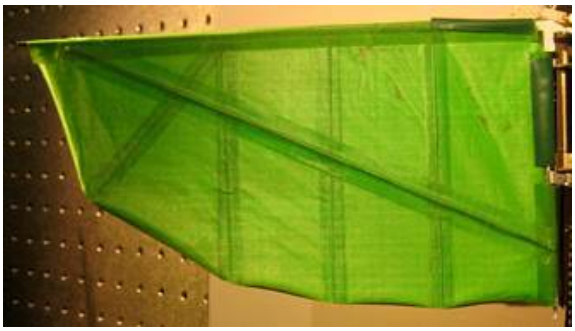

Figure 7. Underside of the kite wing.

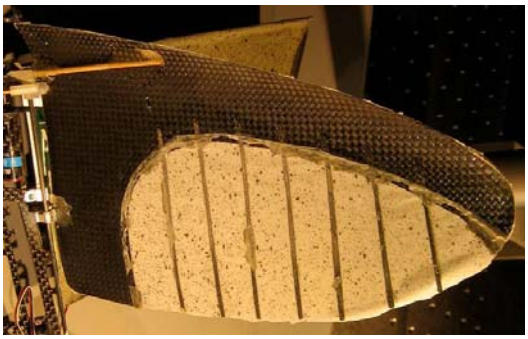

Figure 8. Underside of the latex wing.

The body frame of the vehicle, which is simply a thin carbon fiber frame in the shape of a bird's side profile, is mounted vertically in front of the VIC system. One of the kite wings is removed and replaced by the UF latex wing. Each wing is coated with white paint and speckled with black. When processing a dynamic test, it is essential that data for both the rigid and flexible AOIs are part of the same image file. This is ensured by affixing a rigid plate to the inboard section of the test wing. The plate will act as the rigid AOI. During each test, the wing is attached to an electromagnetic shaker via a rigid rod and universal joint with low friction (see Figure 9). The electromagnetic shaker (Ling Dynamic Systems V201/3-PA 25E) is capable of frequencies up to 13,000 Hz. It acts as a linear actuator to provide the flapping motion. An interface between the linear actuator and a laser doppler vibrometer system allows for several input control signals: sinusoidal, white noise, chirp, and others. A sinusoidal signal is fed to the linear actuator at a user-specified frequency. A load cell (Bruel & Kier 8230) is placed between the structure and the linear actuator, with a sensitivity (of particular concern for light-weight membranes) of 110 mV/N. The cameras were set to record at 100 fps and 1 second's worth of data was processed for each test. Displayed in Table 2 is the test matrix for this experiment. Figure 10 shows the kite wings mounted vertically for a dynamic test and the electromagnetic shaker.

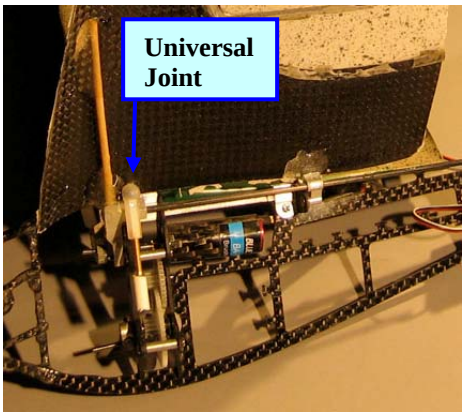

Figure 9. Universal joint and rigid rod affixed to the underside of the latex wing.

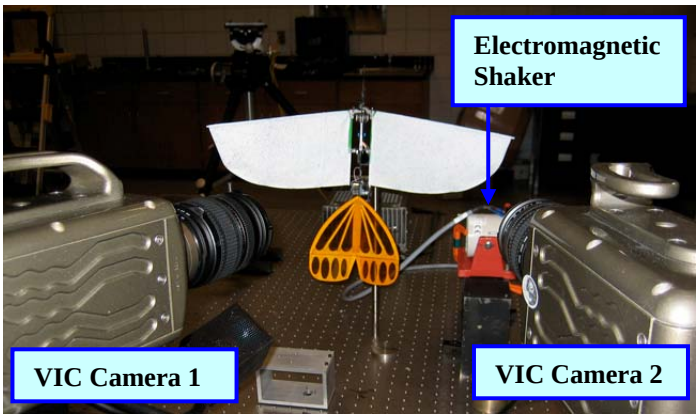

Figure 10. Experimental setup of a dynamic test with the kite wing.

Table 2. Test Matrix for Flapping Wing Experiment

	Input Signal Frequency (Hz)	
Kite Wing	5	10
Latex Wing	5	10

B. Data Post-Processing

Data from the VIC system is post-processed using MATLAB. The VIC data contains the starting position (X, Y, Z) of all data points within the AOI, the corresponding displacements (u,v,w), and other parameters such as the correlation and the in-plane strains. The MATLAB code reads in the data files for both the rigid AOI and flexible AOI. It is important that the rigid AOI files are synchronized with the flexible AOI files; otherwise, the results will not be valid. The HTM is extracted from the rigid AOI data and then applied to the flexible AOI data to get the rigid-body-motion. From that, the elastic deformations are calculated and returned in a series of 2-D and/or 3-D plots. Other outputs of the MATLAB code include the sensitivity of the rotation angles to the

estimated HTM, pooled means and standard deviations for repetition tests, and the location of the maximum deformation for each time step (in the case of dynamic tests).

For post-processing analysis, the angle of the reference frame, i.e. the first frame whose displacements are "0", must be known. For these experiments, the reference frame corresponds to the wing plane being horizontal. This was accomplished by adjusting the wing position to 0° flapping angle. The VIC cameras were commanded to record images prior to the initiation of the flapping motion. The VIC correlation was carried out with the reference frame visually selected as the image just before wing movement.

V. Results

A. Wing Motion

Upon running the algorithm against the four sets of data from the dynamic experiment, the time histories of the flapping angle were obtained (see Figure 11). The flapping angle shown corresponds to the rigid plate. While the input signal into the linear actuator was the same amplitude for each test, the amplitude of the output signal from the load cell was adjusted so as not to exceed its acceleration limits.

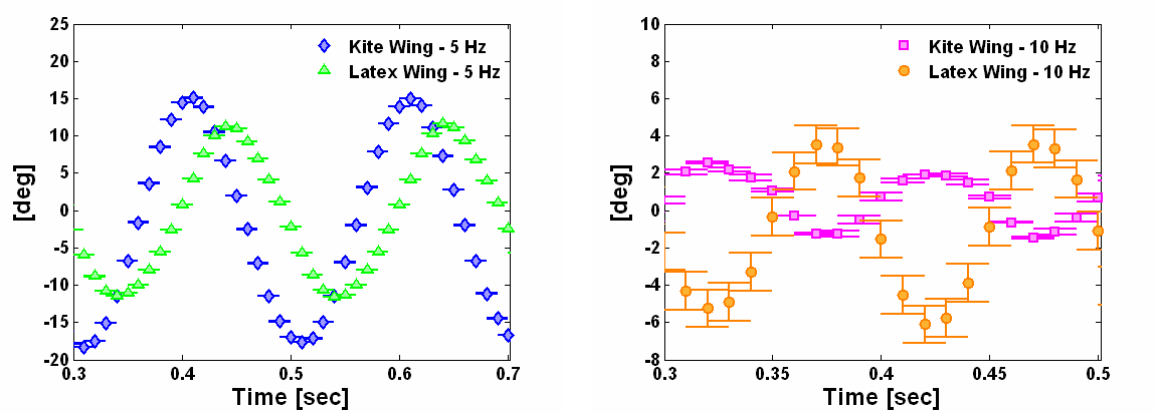

a) 5-Hz input signal **b)** 10-Hz input signal

Figure 11. Time history of the flapping angle, Γ, during the dynamic test.

The plots in Figure 11 include confidence intervals for the values of the flapping angle. These confidence intervals are based on the uncertainty in both the displacement measurements and the coefficients of the HTM. Shown in Table 3 are the displacement uncertainties estimated at 95% probability. Table 4 shows the flapping angle uncertainties based on the error propagation of the measured displacements and estimated HTM. Of particular interest is the rather large uncertainty of 1.01° for the latex wing flapping at 10 Hz compared to the uncertainties of the other wing specimens.

Table 3. Uncertainty in the measured displacements of the kite and latex wings

u_U	u_V	u_W
0.002750	0.000370	0.002890

Table 4. Uncertainty in the flapping angle of the kite and latex wings

	5 Hz	10 Hz
Kite Wing	1.06e-02° (1.86e-04 rad)	8.94e-03° (1.56e-04 rad)
Latex Wing	1.68e-03° (2.93e-05 rad)	1.01° (1.77e-02 rad)

B. Uncertainty in Rotation Angle Estimates

Recall that in the previous section, it was mentioned care should be taken as to which columns of the HTM are used for calculating the rotation angles. This is because of the nature in which the coefficients of the HTM are arrived at. Since a least-squares regression is used, coefficients pertaining to very small numbers (i.e. small X, Y, or Z coordinates) will have a larger uncertainty (refer to Eqn. 9). Presented in Eqn. 10 is the build-up of

the rotational angle uncertainties, taking into account the sensitivity, θ_{HTM}, of the angle to the HTM coefficients from which it was derived,

$$u_{HTM} = \begin{bmatrix} u_U/X & u_U/Y & u_U/Z & u_U \\ u_V/X & u_V/Y & u_V/Z & u_V \\ u_W/X & u_W/Y & u_W/Z & u_W \\ - & - & - & - \end{bmatrix} \tag{9}$$

$$u_\Theta = \pm\left[\left(\theta_{HTM_{22}} u_{HTM_{22}}\right)^2 + \left(\theta_{HTM_{32}} u_{HTM_{32}}\right)^2\right]^{1/2}$$

$$u_\Psi = \pm\left[\left(\theta_{HTM_{12}} u_{HTM_{12}}\right)^2 + \left(\theta_{HTM_{22}} u_{HTM_{22}}\right)^2 + \left(\theta_{HTM_{32}} u_{HTM_{32}}\right)^2 + \left(\theta_{HTM_\Theta} u_\Theta\right)^2\right]^{1/2} \tag{10}$$

$$u_\Gamma = \pm\left[\left(\theta_{HTM_{11}} u_{HTM_{11}}\right)^2 + \left(\theta_{HTM_{21}} u_{HTM_{21}}\right)^2 + \left(\theta_{HTM_{31}} u_{HTM_{31}}\right)^2 + \left(\theta_{HTM_\Theta} u_\Theta\right)^2 + \left(\theta_{HTM_\Psi} u_\Psi\right)^2\right]^{1/2}$$

For the kite wing flapping at 5 Hz, the rigid AOI had very small values for Z and relatively large values for X and Y. This resulted in a large uncertainty for all coefficients in the 3rd column of the HTM; hence the reason for using the first two columns to calculate the rotation angles (see Eqn. 11). However, not every test case had the largest uncertainties in the 3rd column of the HTM. For instance, the latex wing flapping at 10 Hz showed the largest uncertainties to be in the first column (see Eqn. 12). Ideally, the code should perform an uncertainty analysis of the HTM matrix and determine the appropriate coefficients for calculating the rotational angles. This check will be added to the algorithm for future applications.

$$u_{HTM,K5} = \begin{bmatrix} 0.000321 & 0.001649 & 0.341000 & 0.001820 \\ 0.000736 & 0.003780 & 0.780000 & 0.004160 \\ 0.000179 & 0.000917 & 0.190000 & 0.001010 \\ -- & -- & -- & -- \end{bmatrix} \tag{11}$$

$$u_{HTM,L10} = \begin{bmatrix} 0.016800 & -1.71e-05 & 0.007940 & 0.002750 \\ -0.002260 & 2.30e-06 & -0.001070 & -0.000370 \\ -0.017700 & 1.08e-05 & -0.008360 & -0.002890 \\ -- & -- & -- & -- \end{bmatrix} \tag{12}$$

C. Wing Deformation

The estimated wing deformations and projected rigid-body-motions are presented below, grouped according to the type of wing. Figure 12a – 12b show contour plots of the kite wing at 5-Hz flapping frequency and Figure 12c – 12d pertain to a 10-Hz flapping frequency. The contours capture the wing deformation during the start of the upstroke (see Figure 12a and 12c) and the start of the downstroke (see Figure 12b and 12d). Since the kite material does not stretch, its deformation is solely out-of-plane, lending a unidirectional appearance to the contour plots. The larger flapping frequency, though limited by a smaller flapping angle, had larger wing deformation: ±12 mm for the 10-Hz frequency versus ±6 mm for the 5-Hz. It was noted that in Figure 12a - 12b, the top edge of the contour plots, which is near the wing leading edge, experienced deformation. Further investigation showed the measured displacement of the wing to have a feather angle offset from that of the projected rigid-body-motion (see Figure 13).

Results for the latex wing are shown in Figure 14 and Figure 15, following the same layout as that used with the kite wing. Unlike the kite wing, which does not stretch, the latex wing is elastic such that its deformation is both in-plane and out-of-plane. This generates the rounded contour bands seen in Figure 14. Just as with the kite wing, the larger flapping frequency was limited by a smaller flapping angle but had larger wing deformations. Wing twist is also observed as shown by the non-zero deformation along the leading edge of the contours. Figure 15 displays the combined wing twist and elastic deformation occurring at the 10-Hz flapping frequency.

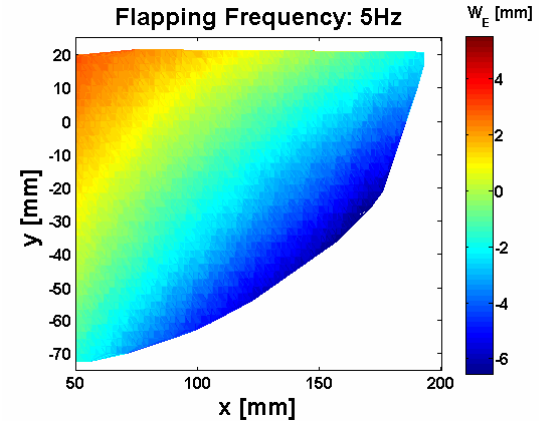

a) Start of upstroke (5 Hz signal)

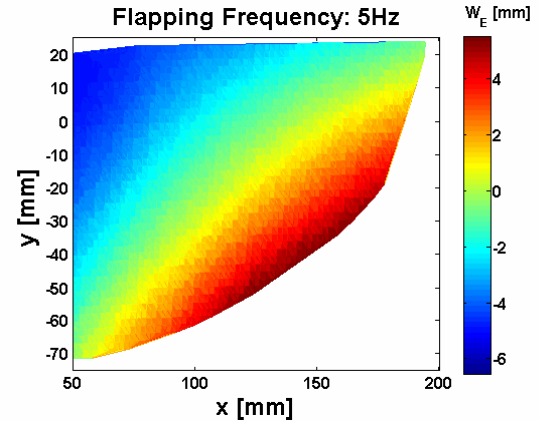

b) Start of downstroke (5 Hz signal)

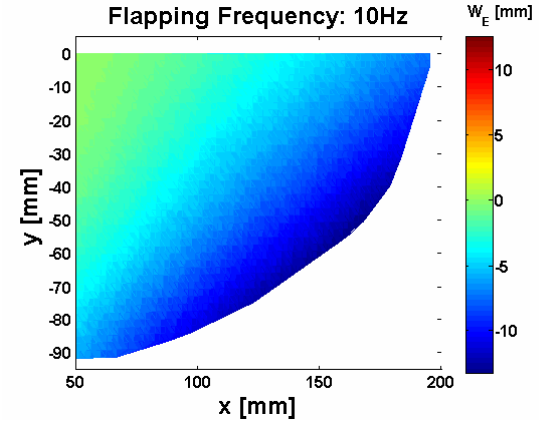

c) Start of upstroke (10 Hz signal)

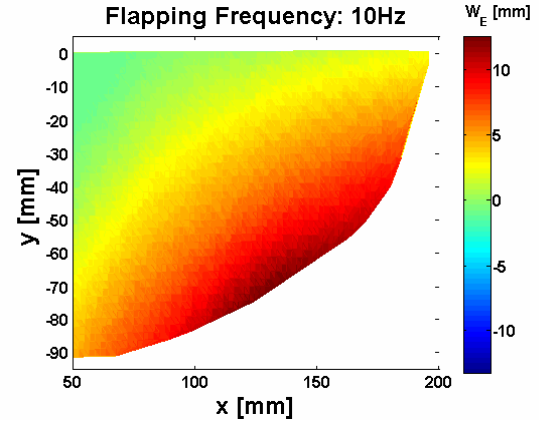

d) Start of downstroke (10 Hz signal)

Figure 12. Upstroke and downstroke contour plots for the kite wing.

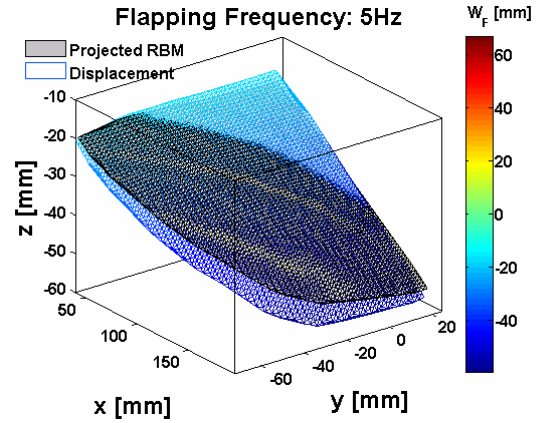

a) Start of upstroke (5 Hz signal)

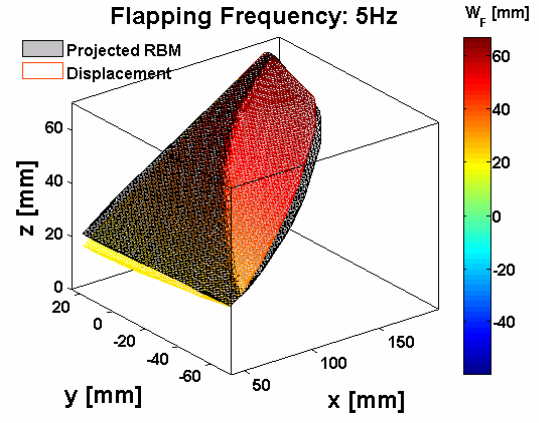

b) Start of downstroke (5 Hz signal)

Figure 13. Measured displacement of the kite wing plotted against the projected-rigid-body motion.

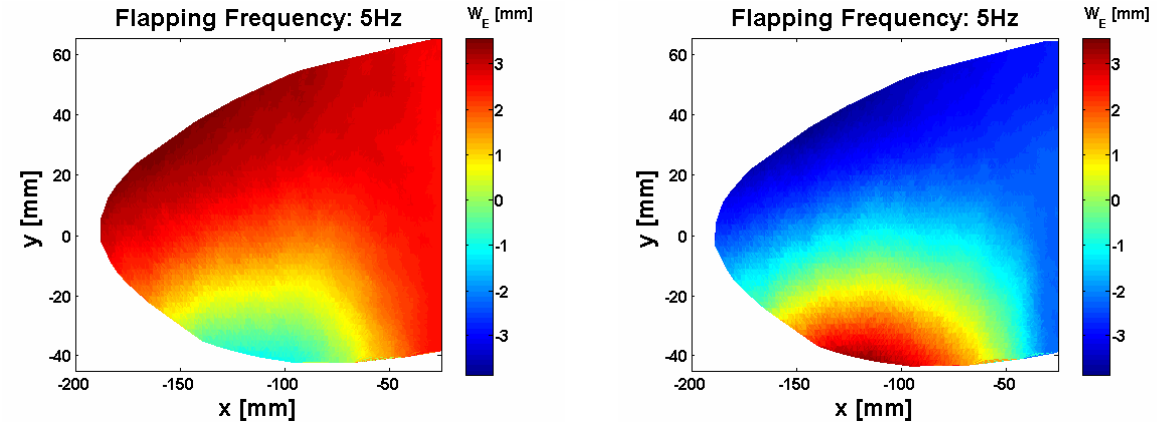

a) Start of upstroke (5 Hz signal) **b)** Start of downstroke (5 Hz signal)

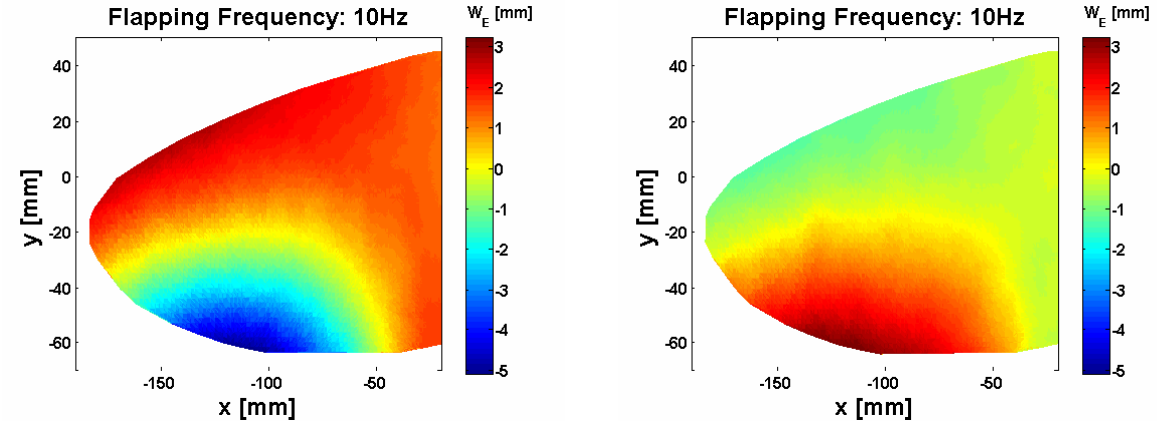

c) Start of upstroke (10 Hz signal) **d)** Start of downstroke (10 Hz signal)

Figure 14. Upstroke and downstroke contour plots for the latex wing.

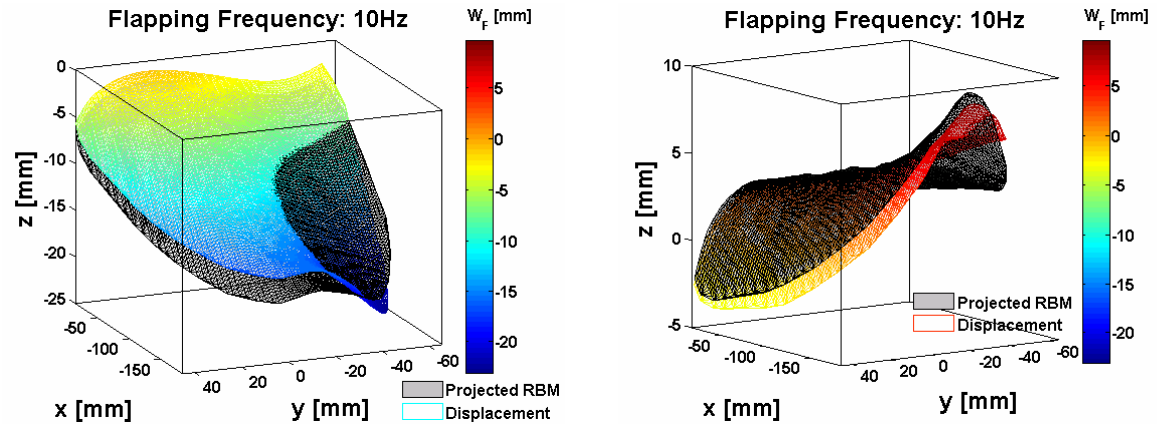

a) Start of upstroke (10 Hz signal) **b)** Start of downstroke (10 Hz signal)

Figure 15. Projected rigid-body-motion plotted against measured displacement for the latex wing.

VI. Conclusions

A method for decoupling the kinematics of wing motion from the deformation of a flapping wing using measurements from a dynamic VIC system was tested and validated. The method constructed the homogeneous transformation matrix from the motion of a rigid plate affixed to the wing and then projected that motion to the area-of-interest. This provided a straightforward means of subtracting the rigid-body-motion from the total displacement of the wing, thereby acquiring the wing deformation.

Application of this decoupling method to test data from a flexible, flapping-wing provided a time history of the flapping angle. Errors in the estimated flapping angle ranged from 1.06e-02° to 1.01°, indicating that a careful check of the uncertainties in the HTM should be carried out prior to the estimation of the projected rigid-body-motion. The method was able to provide contour plots depicting the elastic quality of the latex wing, which experienced both in-plane and out-of-plane deformations, versus the kite wing which experienced out-of-plane deformations only. Wing twist was also captured in the estimated deformations.

Future work with this decoupling method will involve using the dynamic VIC in conjunction with wind tunnel testing. This method will be useful for gaining insight into the mechanics and flow-structure interactions that occur with flapping motion and possibly lead to a better understanding of how wing flexibility effects the lift and thrust characteristics in flapping wings.

Acknowledgements

This work was supported by the Research Institute for Autonomous Precision-Guided Systems under grants F49620-03-1-0170 and FA9550-07-1-0236 with Dr. Fariba Fahroo as the project monitor. The authors would also like to acknowledge the technical contributions of Dr. Nick Gans at the Research and Engineering Education Facility, Shalimar FL.

References

[1] Raney, D. L., and Waszak, M. R., "Biologically-Inspired Micro-Flight Research", SAE Paper 2003-01-3042, World Aviation Conference and Exposition, September 2003.

[2] Raney, D. L., and Slominski, E. C., "Mechanization and Control Concepts for Biologically-Inspired Micro Aerial Vehicles", AIAA Paper 2003-5345, Guidance, Navigation, and Control Conference, August 2003.

[3] Fish, F., Nusbaum, M., Beneski, J., and Ketten D., "Passive Cambering and Flexible Propulsors: Cetacean Flukes", *Bioinspiration and Biomimetics*, Vol. 1, 22 Dec. 2006, pp. 42 – 48.

[4] Albertani, R., Stanford, B., Hubner, J. P., and Ifju, P.G., "Aerodynamic Coefficients and Deformation Measurements on Flexible Micro Air Vehicle Wings", Mechanical and Aerospace Engineering Department, University of Florida, Gainesville, FL, 2007.

[5] Tian, X., Iriarte-Diaz, J., Middleton, K., Galvao, R., Israeli, E., Roemer, A., Sullivan, A., Song, A., Swartz, S., Breuer, K., "Direct Measurements of the Kinematics and Dynamics of Bat Flight", *Bioinspiration and Biomimetics*, Vol. 1, 22 Dec. 2006, pp. 10 – 18.

[6] Hoa, S., Nassefa, H., Pornsinsirirakb, N., Taib, Y., Hoa, C., "Unsteady Aerodynamics and Flow Control for Flapping Wing Flyers", *Progress in Aerospace Sciences*, Vol. 39, 2003, pp. 635 – 681.

[7] Pennycuick, C. J., Lock, A., "Elastic Energy Storage in Primary Feather Shafts", *Journal of Experimental Biology*, Vol. 64, 1976, pp. 667 – 689.

[8] Sutton, M. A., Cheng, M., Peters, W. H., Chao, Y. J., McNeill, S. R., "Application of an Optimized Digital Correlation Method to Planar Deformation Analysis", *Image and Vision Computing*, Vol. 4, No. 3, 1986, pp. 143 – 150.

[9] Sutton, M. A., Turner, J. L., Bruck, H. A., Chae, T. A., "Full-field Representation of the Discretely Sampled Surface Deformation for Displacement and Strain Analysis", Experimental Mechanics, Vol. 31, No. 2, 1991, pp. 168 – 177.

[10] Critchlow, A. J., *Introduction to Robotics*, MacMillan Publishing Company, New York, 1985, pp. 178 – 197.